Quasi-one-dimensional magnetic properties of NiNb2–xVxO6 compounds synthesized at high pressure in a nonstandard columbite-type structure

J Peña, M A Gusmão, O Isnard

Quasi-one-dimensional magnetic properties of $NiNb_{2-x}V_xO_6$ compounds synthesized at high pressure in a nonstandard columbite-type structure

J. Peña [1,2,*] M. A. Gusmão [2] and O. Isnard [1]

[1] *Université Grenoble Alpes, CNRS, Institut Néel, 25 rue des Martyrs Boîte Postale 166, 38042 Grenoble, France*

[2] *Universidade Federal do Rio Grande do Sul, Instituto de Física, Av Bento Gonçalves 9500, 91501-970 Porto Alegre, Brazil*

(Received 14 August 2020; revised 6 November 2020; accepted 18 February 2021; published 4 March 2021)

We report on the low-dimensional magnetic behavior of the series of compounds $NiNb_{2-x}V_xO_6$ ($0 \leqslant x \leqslant 2$), with a columbite-type crystal structure stabilized at high pressure and temperature. Based on susceptibility, magnetization, and specific-heat measurements, the system is characterized as presenting quasi-one-dimensional magnetism, with Ni^{2+} magnetic moments that can be modeled as Ising spins, placed along zigzag chains in the crystal structure. The low-temperature phase is found to consist of an antiferromagnetic arrangement of ferromagnetic chains, and a metamagnetic transition to uniform ferromagnetic order is observed under magnetic fields slightly above $\mu_0 H = 1$ T. We discuss the effects of substituting vanadium for niobium, maintaining the same crystal structure along the whole series of samples. In particular, the long-range magnetic order, most clearly seen for $x = 0$, tends to be suppressed as the vanadium content is increased. The exchange interactions are quantified, revealing that the ferromagnetic intrachain interactions vary from about 7 K for $NiNb_2O_6$ to 2 K for NiV_2O_6, remaining one order of magnitude larger than the mean antiferromagnetic interchain coupling.

DOI: 10.1103/PhysRevB.103.094409

I. INTRODUCTION

The diversity of physical properties observed in compounds of the AB_2O_6 system is directly linked to the different possible structures in which they crystallize. In this system, A is a divalent metallic ion while B is a nonmagnetic pentavalent metal of the fifth group. Subfamilies of the AB_2O_6 compounds are called tantalites, niobates, or vanadates when $B =$ Ta, Nb, or V, respectively. In general, the symmetry of the unit cell in room-pressure synthesized compounds is reduced from tetragonal in the tantalites to orthorhombic in the niobates, and triclinic in the vanadates. However, the A cations also play an important role in determining the structure of each specific compound. Concerning magnetic properties, long-range magnetic ordering in tetragonal tantalites has been described by two-dimensional models of Heisenberg spins with single-ion anisotropy [1–3], while quasi-one-dimensional Ising-like magnetism successfully models the orthorhombic niobates [4–8]. The Ising model, as in all real systems, is a good approximation in the presence of strong spin anisotropy of the type DS_z^2, with the origin on the spin-orbit interaction associated with quenching of the orbital angular momentum in the crystal field. Here we focus on a description of magnetism in the series of compounds $NiNb_{2-x}V_xO_6$, which we obtain in the orthorhombic columbite-type structure of the *Pbcn* space group by synthesis in extreme conditions of pressure and temperature.

In general, the transition metal niobates, ANb_2O_6, crystallize in the columbite-type structure, while the vanadates, AV_2O_6, may present several polymorphs depending on the A ion. For example, MnV_2O_6 is monoclinic and crystallizes in the $C2/m$ space group [9]. On the other hand, depending on the temperature of synthesis, CoV_2O_6 can be monoclinic (α phase) or triclinic (γ phase) [10–12]. The structure is unequivocally triclinic when $A =$ Ni,Cu. Here we use the niobate $NiNb_2O_6$ as the reference compound of the series.

$NiNb_2O_6$ is formed by successive layers of oxygen octahedra surrounding the Ni^{2+} and Nb^{5+} cations. The octahedra around Ni^{2+} ions are distorted, and they are arranged in zigzag edge-sharing chains parallel to the c axis. Along the a axis, NiO_6 and NbO_6 octahedra form an alternating sequence NiNbNbNi...[13]. The magnetic moments of Ni^{2+} ions lie on the ac plane, forming ferromagnetic (FM) zigzag chains, with a spin easy axis canted by approximately 31° with respect to the crystallographic c axis [14]. The Ni^{2+} chains intercept the ab plane at points arranged in an isosceles triangular geometry. These chains are antiferromagnetically coupled in the transverse directions. Such coupling would be frustrated in a regular triangular geometry, but this is not so with isosceles triangles, allowing for different spin patterns. Two coexisting magnetically ordered phases, with propagation vectors $(0, 1/2, 0)$ and $(1/2, 1/2, 0)$, have been reported [8,14,15]. Dislocations causing local strain or surface effects can favor one or the other, producing magnetic domains of these phases even in single crystals. In the analogous compound $CoNb_2O_6$, the one-dimensional character of the Co^{2+} chains dominates the magnetic behavior. In that case, interchain interactions yield a sequence of transitions, first to a three-dimensional incommensurate antiferromagnetic (AF) ordering at a temperature $T_N^{(inc)} \sim 2.9$ K, and then, at $T_N \sim 1.9$ K, to a coexistence of two AF phases with propagation vectors $(0, 1/2, 0)$ and $(1/2, \pm 1/2, 0)$, the first one being dominant (∼80%) [7]. In $NiNb_2O_6$, the larger orthorhombic distortion leads to weaker

*jully.pena-pacheco@neel.cnrs.fr

competition of the interchain interactions, so that a transition occurs, at $T_N = 5.7$ K, directly to the coexistence of the two AF phases described above [8,14,15]. In all cases, the FM superexchange intrachain interactions along the c axis are the strongest ones.

NiV_2O_6, at the other extreme of the series, when synthesized at room pressure, crystallizes in a triclinic structure of the $P\bar{1}$ group, exhibiting a paramagnetic-antiferromagnetic transition at $T_N = 16.4$ K [16]. As in the columbite structure, in triclinic NiV_2O_6 the edge-connected NiO_6 octahedra also give rise to chains along the c axis, with FM interactions of moderate strength, as revealed by a positive $\Theta_{CW} = 7.6$ K. In this case, the planes containing chains of NiO_6-octahedra are separated by two planes of alternated octahedral and tetrahedral arrangements of oxygen atoms around the V^{5+} ions. This structure also shows two-dimensional long-range antiferromagnetism due to interactions between the Ni^{2+} chains.

Even though the AB_2O_6 compounds have been known for a long time, the fact that crystal structure is as important as chemical composition to determine their physical properties allows for new characteristics to still be revealed in these materials. For example, it was recently discovered that the *Pbcn*-MnV_2O_6 exhibits low-dimensional magnetism below $T_N = 4.7$ K [9,17], while its monoclinic analog shows three-dimensional ordering at temperatures that have been reported between $T_N = 17$ K [18] and $T_N = 24$ K [19]. Apart from magnetic properties, studies on NiV_2O_6 proved it to be a visible-light-active photoanode for photoelectrochemical water oxidation [20]. It was also found that $NiNb_2O_6$ has potential as a photocatalyst under visible-light irradiation for efficient production of H_2 from water splitting [21]. In addition, electrical resistivity changes have been predicted and experimentally observed upon subtle changes in composition or pressure-induced structures of different members of the AB_2O_6 family [22–24].

Motivated by this rich phenomenology, here we explore the evolution of magnetic properties when vanadium is gradually substituted for niobium in the series $NiNb_{2-x}V_xO_6$ ($0 \leqslant x \leqslant 2$), employing high-pressure–high-temperature (HPHT) synthesis to stabilize the columbite-type structure in samples with $x > 0$. Comparison of magnetic properties could thus be done in a set of samples with the same crystal structure, which is hard to find among the vanadates of the AV_2O_6 family.

II. EXPERIMENTAL DETAILS

Samples of $NiNb_{2-x}V_xO_6$ were obtained by submitting stoichiometric mixes of powder $P\bar{1}$-NiV_2O_6 and *Pbcn*-$NiNb_2O_6$ to an external pressure of 5.9 GPa, and simultaneously to temperatures of 900 °C for 60 min ($x \geqslant 1$) or 1100 °C for 20 min ($x = 0.66$). These syntheses were performed in a CONAC-40 press. $NiNb_2O_6$ was synthesized by annealing stoichiometric mixes of high-purity NiO and Nb_2O_5 at 1300 °C for 48 h. The $P\bar{1}$-NiV_2O_6 powder was obtained from a mixture of high-purity Ni-acetate ($NiC_4H_{14}O_8$) and V_2O_5. An excess of 7% in mass of the acetate with respect to the stoichiometrically necessary quantity of V_2O_5 was used in order to avoid formation of an impurity phase of $Ni_2V_2O_7$. The thermal treatment was performed at 620 °C for 48 h.

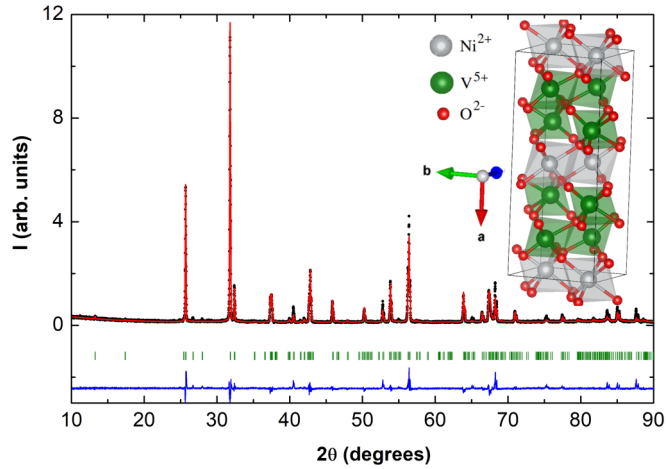

FIG. 1. Refined XRD pattern for the sample NiV_2O_6 recorded at room temperature, showing the experimental data (black points), the calculated curve from Rietveld refinement (red line), the difference between data and fitting (blue line at the bottom), and the expected positions of Bragg peaks for the *Pbcn* space group (green vertical marks). The inset depicts a unit cell of the structure, showing oxygen octahedra surrounding the cations.

Complete recipes for preparation of these samples can be found in Ref. [25].

X-ray diffraction (XRD) patterns were acquired in the Bragg-Brentano geometry, at room temperature, in a Bruker D8 Endeavor diffractometer with a copper anode ($\lambda_\alpha = 1.5418$ Å). The diffraction patterns were refined by the Rietveld method, using the FULLPROF software suite [26].

Measurements of magnetization and magnetic susceptibility on powder samples were performed in a Quantum Design® SQUID magnetometer and in a home-made extraction magnetometer [27]. The temperature and magnetic-field ranges were 1.9–300 K and 5–10 mT.

Specific heat was measured in a Quantum Design® Physical Properties Measurement System, using a small pellet of each sample (mass between 2.5 and 7 mg). Measurements were performed in the range 1.9–300 K, employing the temperature-relaxation method with a 2% increase of the system temperature at each point.

III. RESULTS AND DISCUSSION

A. Crystal structure

Rietveld refinement of the XRD patterns indicates that all samples of our $NiNb_{2-x}V_xO_6$ series crystallized in structures of the *Pbcn* space group. Except for the sample with $x = 0.66$, the Rietveld refinement was successfully achieved by taking into account a single phase with nominal stoichiometry, which indicates that these samples are formed by a single structural phase. An example of a refined pattern, for the sample NiV_2O_6, is shown in Fig. 1. Several attempts were made to obtain a single phase with $NiNb_{1.5}V_{0.5}O_6$ stoichiometry. However, in all attempts it was necessary to allow for the presence of $NiNb_2O_6$ in order to complete the refinement. The best result was obtained for the sample identified here as $x = 0.66$, in which the "impurity" phase ($NiNb_2O_6$) represents 27% of

TABLE I. Structural parameters derived from Rietveld refinements of XRD patterns at room temperature in the series of samples $NiNb_{2-x}V_xO_6$. The unit-cell parameters are listed in the first four rows. The next five rows show the intrachain parameters, Ni-O-Ni angle (θ), mean Ni-O distance ($\langle d_{\text{Ni-O}}\rangle$), and Ni-Ni distance along the c axis, followed by the shortest interchain Ni-Ni distances, along the a axis and away from the c direction on the bc-plane. The last two rows present the agreement parameters of Rietveld refinement.

x	0	0.66	1	1.5	2
a (Å)	14.0229(2)	13.8158(4)	13.7013(3)	13.5013(4)	13.3518(2)
b (Å)	5.6769(1)	5.6375(2)	5.6121(1)	5.5649(2)	5.5252(1)
c (Å)	5.0184(1)	4.9611(1)	4.9253(1)	4.8639(1)	4.8145(1)
V (Å^3)	399.51(1)	386.40(2)	378.72(1)	365.44(2)	355.166(8)
θ (deg)	100.1(4)	95.1(2)	95.1(5)	95.6(5)	90.5(4)
$\langle d_{\text{Ni-O}}\rangle$ (Å)	1.990(4)	2.012(1)	2.073(4)	2.078(4)	2.077(4)
$(\text{Ni-Ni})_c$ (Å)	3.106(3)	3.076(4)	3.081(4)	3.060(4)	2.957(3)
R_P (%)	9.07	7.16	6.72	7.13	9.71
R_{WP} (%)	11.5	9.24	9.30	9.77	12.4

the total mass. With this, we deduced that the main phase, with a higher concentration of vanadium than initially intended, corresponds to the chemical formula $NiNb_{1.34}V_{0.66}O_6$.

Structural information obtained by XRD on the series $NiNb_{2-x}V_xO_6$ studied here is presented in Table I. As the vanadium content increases from $x = 0$ to 2, the lattice parameters a, b, and c of the *Pbcn*-$NiNb_{2-x}V_xO_6$ samples are reduced by 4.8%, 2.7%, and 4.1%, respectively, as can be seen in Table I. The same relative changes were found in Refs. [9,17] for the lattice parameters of $MnNb_2O_6$ and MnV_2O_6. This indicates a remarkably anisotropic response of the atomic arrangement to chemical substitution at the B-site in both systems.

A noticeable distinction between $NiNb_2O_6$ and its isomorph compound NiV_2O_6 is the large difference in the Ni-O-Ni angle in zigzag chains. This angle is close to 90° in the pure vanadate, and it increases to around 95° in the intermediate compounds, achieving 100° in the niobate. Thus, it is clear that reduction of the bonding angle is a key feature to adapt the *Pbcn*-columbite crystal structure to the specific characteristics of the V^{5+} cation, like its smaller ionic radius in comparison to Nb^{5+}. This large angular change contrasts with the regularly progressive evolution of the lattice parameters occurring along the $NiNb_{2-x}V_xO_6$ solid solution. A comprehensive study of the structure and Raman spectrum of this same series of samples is reported in Ref. [25].

B. Magnetic susceptibility

Magnetic susceptibility (χ) as a function of temperature was measured for all the samples, with an applied magnetic field $\mu_0 H = 10$ mT. As an example, the curve for sample $x = 1.5$ is shown in Fig. 2, where the inset shows the temperature derivative of the product χT. The maximum of $d(\chi T)/dT$, which occurs below the peak-temperature (T_p) on the χ versus T diagram, is the actual location of the PM-AF transition, where the Néel temperature T_N is defined. Both T_p and T_N are reported in Table II for all the studied samples. The $x = 0.66$ sample presents two peaks, both in the susceptibility and in the derivative of χT. The higher-temperature peaks correspond to the secondary phase of pure $NiNb_2O_6$, so that the lower-temperature ones are deduced as being due to the main phase $NiNb_{1.34}V_{0.66}O_6$, and they are the only ones listed for this composition in Table II. The Néel temperature in this case is reduced by nearly 50% with respect to $NiNb_2O_6$, remaining at this level, with small variations, for all samples with vanadium. A peak in the susceptibility is clearly visible in all cases, but the one on the $d(\chi T)/dT$ curve becomes quite rounded out, to recover some sharpness only for NiV_2O_6. From these results, it is clear that the stability of the long-range magnetic ordering is substantially reduced when even small quantities of V atoms are substituted for Nb.

We also analyzed the high-temperature behavior of the magnetic susceptibility, by fitting inverse-susceptibility data to the Curie-Weiss law, $\chi^{-1} = C^{-1}(T - \Theta_{\text{CW}})$, in the region $T > 50$ K, as shown in Fig. 3. The resulting values of Curie-Weiss temperature (Θ_{CW}) and Curie constant (C) for all the samples are included in Table II. To enhance the signal in the paramagnetic state, these measurements were performed at a relatively high applied magnetic field, $\mu_0 H = 2$ T. Except for the $x = 0$ sample, a linear behavior of the inverse susceptibility at high temperatures was only obtained after subtracting a very small temperature-independent magnetic moment (of order 10^{-6} emu) from the raw data. Interestingly,

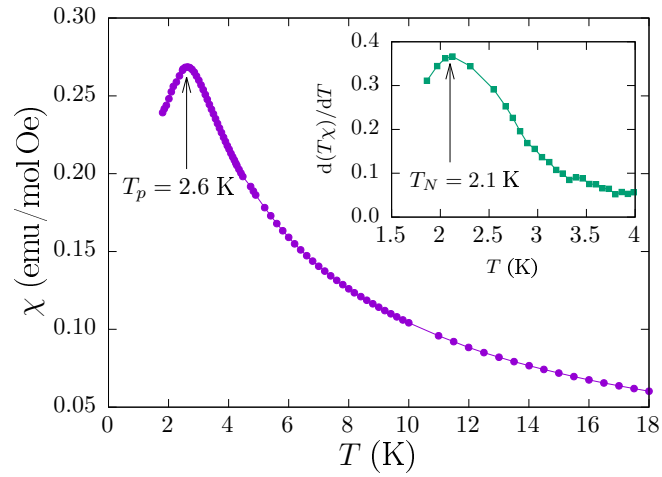

FIG. 2. Magnetic susceptibility as a function of temperature for $NiNb_{0.5}V_{1.5}O_6$ with a measuring field $\mu_0 H = 10$ mT. The inset shows the temperature derivative of the product $T\chi$, whose peak is used to define T_N.

TABLE II. Magnetic parameters obtained from the analysis of magnetic susceptibility and magnetization of the *Pbcn*-$NiNb_{2-x}V_xO_6$ samples studied here. The exchange constants J_0 and $J_\perp$ are defined in the text in connection with Eqs. (1) and (2). The saturation magnetization M_s is discussed in Sec. III C.

x	0	0.66	1	1.5	2
T_p (K)	6.5	3.5	2.9	2.6	3.0
T_N (K)	5.7	2.9	2.4	2.1	2.5
Θ_{CW} (K)	12.5	6.9	4.1	2.3	2.3
C (emu K/mol Oe)	1.33	1.31	1.29	1.27	1.21
μ_{eff} (μ_B/Ni^{2+})	3.29	3.24	3.20	3.18	3.11
J_0 (K)	7.12	4.40	3.14	2.22	2.38
$J_\perp$ (K)	−0.29	−0.32	−0.36	−0.36	−0.40
M_s (μ_B/f.u.)	2.2	1.87	1.93	2.08	1.7

this constant moment is positive, with its value depending on the measuring field, which indicates the presence of Van Vleck paramagnetism in the samples containing vanadium. The role of vanadium is to change the crystal field acting on Ni^{2+} ions, which is responsible for the anisotropy and the Van Vleck term. This is consistent with the observed increase of Ni-O distance with increasing vanadium content (see Table I). It should be noticed, both in Fig. 3 and in Table II, that Θ_{CW} is positive, indicating a dominance of intrachain FM interactions in the PM phase. However, the strong reduction of its value in the substituted samples with respect to the pure-Nb one reveals a weakening of these interactions as the vanadium content increases.

The effective magnetic moment was calculated from the Curie constant through the relation $C = \mathcal{N}\mu_{eff}^2/3k_B$, where $\mathcal{N}$ is the appropriate density of magnetic moments (Avogadro's

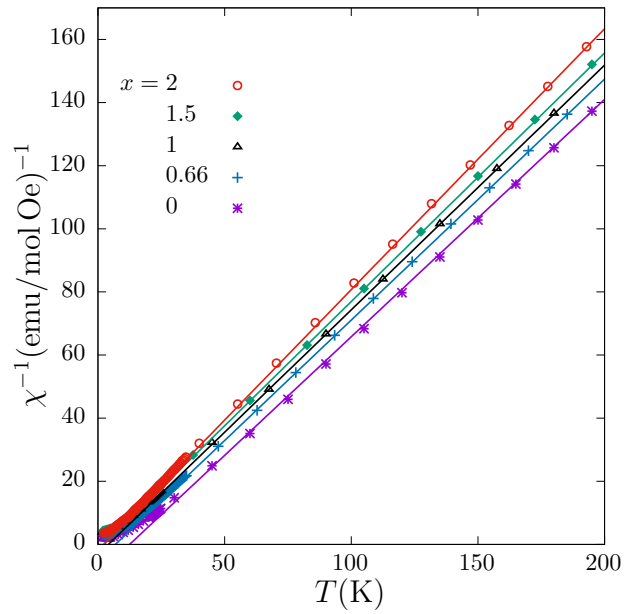

FIG. 3. Inverse of the magnetic susceptibility as a function of the temperature for all the samples of the series $NiNb_{2-x}V_xO_6$. Symbols represent experimental data taken at $\mu_0 H = 2$ T, while lines are fittings to the Curie-Weiss law.

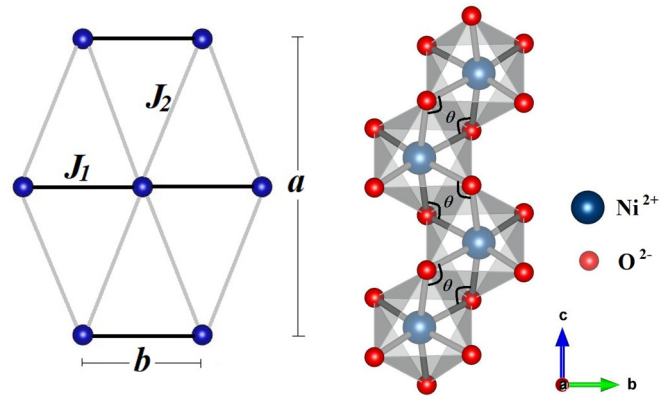

FIG. 4. Left: Magnetic interchain exchange interactions (J_1, J_2) and unit-cell parameters on the *ab*-plane of the *Pbcn* columbite-type structure. Blue spheres represent Ni^{2+} cations. Right: Schematic representation of a chain of oxygen octahedra surrounding Ni ions along the *c* axis, indicating the Ni-O-Ni angle θ quoted in Table I.

number, for the susceptibility units used here). One should note that the factor 1/3 in this relation between C and μ_{eff} would not be expected for Ising spins. However, in a polycrystalline system we must take into account the field component along the anisotropy axis, which may be denoted as $H\cos\theta$. Then, the overall susceptibility involves the average $\langle\cos^2\theta\rangle$ over half of a solid angle, also yielding a factor 1/3. The value $\mu_{eff} \sim 3.3\mu_B/Ni^{2+}$ found here agrees with that obtained in Ref. [8] for $NiNb_2O_6$, and is very similar to the one reported for $P\bar{1}$-NiV_2O_6 ($3.24\mu_B/Ni^{2+}$) in Ref. [16]. We see in Table II that μ_{eff} remains essentially the same along the whole series of $NiNb_{2-x}V_xO_6$ samples. This indicates that the valence and spin state of Ni^{2+}-cations remain unchanged throughout the series, but also that the *g*-factor does not vary significantly. This value is quite large since the Ni spin should be $S = 1$. It was verified in Ref. [17] that the effective magnetic moment of Mn^{2+} ions also remains unaltered when the structure passes from monoclinic to orthorhombic. Thus we can conclude that in general the local structural changes around A^{2+} cations in the AB_2O_6 compounds do not affect the crystal field enough to alter their effective magnetic moments.

To estimate values of exchange constants in the studied compounds, we employ a theoretical approach described in Ref. [28]. It combines the exact susceptibility of a one-dimensional Ising model to account for the intrachain interactions J_0 with a mean-field approximation to include an interchain exchange $J_\perp$. The latter is actually an average of two couplings, J_1 and J_2, due to the existence of two different distances between chains, as schematically represented on the left-hand side of Fig. 4. The magnetic susceptibility is then given by

$$\chi = \frac{C}{\chi_0^{-1} - z_\perp J_\perp}, \tag{1}$$

where

$$\chi_0 = \frac{1}{T}\, e^{2J_0/T} \tag{2}$$

is the exact per-spin susceptibility of an isolated Ising chain, $z_\perp = 6$ is the number of neighboring chains, and the value

$S = 1$ was explicitly taken for the spin of Ni^{2+} cations. The values of J_0 and $J_\perp$ (implicitly divided by Boltzmann's constant k_B) were found by fitting the experimental susceptibility data to Eq. (1). This was done enforcing the constraint $\Theta_{CW} = (2J_0 + z_\perp J_\perp)S^2$, which is easily obtained by expanding the exponential in χ_0^{-1} to first order, and using the Θ_{CW} values found in our Curie-Weiss fittings of the susceptibility. The temperature range for this fitting begins slightly above the susceptibility maximum since the mean-field approximation for the interchain interaction is not able to reproduce this maximum nor the reduction to zero at lower temperatures. We see in Eqs. (1) and (2) that the interchain part cuts off the divergence of χ_0 as $T \to 0$, stabilizing χ at the limit $C/z_\perp|J_\perp|$.

The results for J_0 and $J_\perp$ are listed in Table II. It is worth remarking that J_0 is always at least one order of magnitude larger than $J_\perp$. Nevertheless, there is a reduction of J_0 with increasing vanadium content. This quantifies our previous discussion on the variation of the Curie-Weiss temperature as x goes from 0 to 2 in the series $NiNb_{2-x}V_xO_6$. We may interpret the weakening of J_0 in light of structural changes revealed by the atomic distances quoted in Table I. There we see that the Ni-Ni distance along the chain (axis c) is reduced while the Ni-O distance increases, both consistent with the observed reduction of the Ni-O-Ni angle. These changes can be better understood through the schematic representation of a Ni chain shown on the right-hand side of Fig. 4. Ni-Ni coupling along the chain occurs through oxygen ions located at the corners of shared edges of the octahedra. Such a cation-anion-cation superexchange is FM when the bond angle is about 90° [29], as is the case here. Thus, the reduction of J_0 with vanadium content may be attributed to the increase in Ni-O distance, quoted in Table I as an average over all the oxygens surrounding a Ni ion.

Turning now to the interchain exchange, Table II shows that the absolute value of $J_\perp$ increases as the vanadium content goes from $x = 0$ to 2. Since this is the interaction ultimately responsible for the establishment of an ordered state, we should expect higher Néel temperatures in the vanadium-rich compounds. However, this seems to be counterbalanced by the weakening of the intrachain interaction, which reduces the tendency to order in the chain, resulting in a reduction of the Néel temperature. We may also expect frustration effects due to a certain amount of disorder in the substitution of V for Nb. Such a disorder due to inhomogeneous insertion of V atoms in the $NiNb_2O_6$ matrix is suggested by the evolution of the Raman spectrum along this series of compounds [25]. It is possible that disorder in the interchain interactions partially compensates for the difference between J_1 and J_2 (see Fig. 4), nearly recovering a frustrated triangular network.

C. Isothermal magnetization

Isothermal magnetization curves at $T = 1.8$ K are plotted for all the studied samples in the top panel of Fig. 5. Two different regimes are clearly visible in the magnetization curves of the samples with $x = 0$, 0.66, and 2, with an initial linear growth of $M(H)$, followed by a marked upturn at critical fields between $\mu_0 H \simeq 1.2$ and 1.6 T. This upturn yields peaks in the derivative dM/dH, shown in the bottom panel of the same figure. The peak for $x = 0.66$ is mainly due to the pure niobium phase present in this sample, which has a well-developed magnetization because it is substantially below its Néel temperature. In contrast, the samples with $x = 1$ and 1.5 do not show more than a barely perceptible shoulder in dM/H around $\mu_0 H \gtrsim 1$ T. These samples have T_N's closer to the measuring temperature, besides being possibly affected by composition disorder that may impair long-range order.

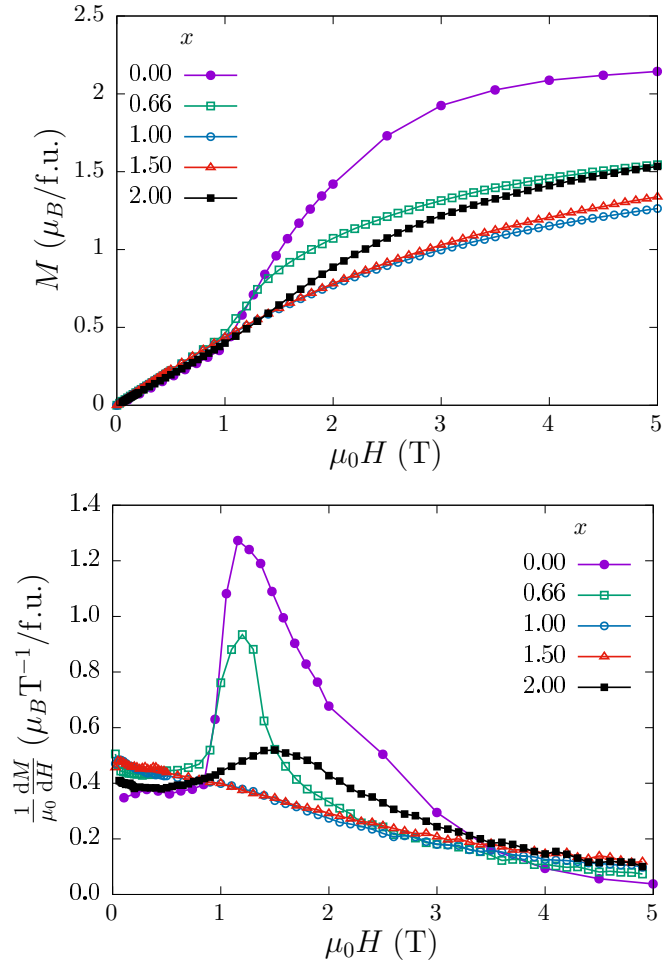

FIG. 5. Isothermal magnetization curves taken at $T = 1.8$ K (top) and their numerical derivatives (bottom) for the indicated samples of the $NiNb_{2-x}V_xO_6$ compounds.

The above-described behavior of $M(H)$ can be interpreted as indicative of spin-flip AF-FM transitions. Such transitions were already observed in samples of $Fe_{1-x}A_xNb_2O_6$ (A = Co,Ni) and were interpreted as being produced when the AF alignment of FM chains is overcome by the magnetic field [8,28], flipping the ones that were oriented in the opposite direction. It is interesting to note that the field necessary to induce this metamagnetic transition in the $x = 2$ sample is clearly larger than in the $x = 0$ one, even though the latter has a higher Néel temperature. This apparent contradiction can be understood by inspecting the values of transition temperatures and exchange parameters quoted in Table II. We see that a higher J_0 favors the establishment of an ordered state, but a higher $J_\perp$ makes it more difficult to overturn one chain against the effective field of the neighboring ones.

Finally, it is worth remarking that an ideal spin-flip transition would involve a finite jump of the magnetization. However, a continuous change, as observed here, should be expected in polycrystalline and/or powder samples due to the random orientation of the applied field with respect to local anisotropy axes.

It is clear in Fig. 5 that only the $x = 0$ sample is close to saturation at $\mu_0 H = 5$ T. To investigate the saturation magnetization (M_s) of our samples, as well as temperature effects on the magnetization curves, we extended the magnetic-field range up to $\mu_0 H = 10$ T. M_s values for all samples were estimated as the extrapolated intersection of the high-field data of M versus $1/H$ with the vertical axis [30]. These values of M_s are listed in Table II. Isothermal magnetization curves at various temperatures are shown in Fig. 6 for the samples with $x = 0$, 1, and 2. We see that even at these higher fields, saturation is reached only in the $x = 0$ sample, with $M_s \simeq 2.2\mu_B$/f.u. The other two show magnetizations still growing, although clearly approaching a limit value close to one-half of the effective moment obtained from the high-temperature susceptibility. This also happens for $x = 1$ and 1.5, and is actually expected for randomly oriented grains in powder samples [12]. The sample holder used in these measurements consisted of a nonmagnetic cylinder that was filled with the sample powder without any type of pressing. Thus, we expect the orientation of the grains with respect to the magnetic field to be random. The higher M_s value for $x = 0$ seems to be indicative of some degree of grain reorientation under strong magnetic field. This is consistent with the stronger intrachain exchange in this case, which should yield larger chain moments.

It is interesting to note in Fig. 6 that we can see upturns of the magnetization curves at the fields corresponding to the metamagnetic transition, but only for temperatures below T_N, as expected. The change of slope occurs up to $T = 5$ K for $NiNb_2O_6$, and at $T = 1.7$ K but not at 3 K or above for NiV_2O_6, in agreement with the respective Néel temperatures of 5.7 and 2.5 K quoted in Table II. The field-induced transition is not visible in the isothermal magnetization curves for $NiVO_6$, as already noted in Fig. 5.

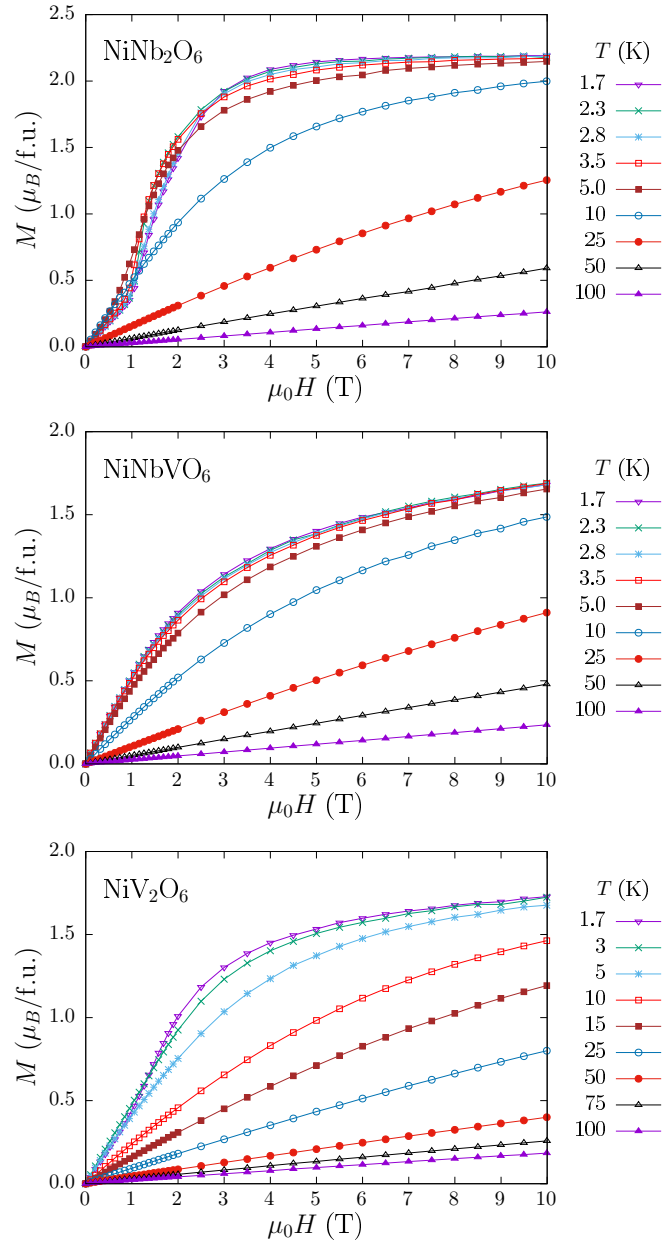

FIG. 6. Isothermal magnetization curves for $NiNb_2O_6$ (top), $NiNbVO_6$ (center), and NiV_2O_6 (bottom), at the quoted temperatures.

D. Specific heat

Measurements of specific heat as a function of temperature were performed for all the samples studied here. Raw data for samples with $x = 0$ and 2 are presented in the top panel of Fig. 7. A clear peak marking the magnetic transition only appears for $x = 0$, and just a broad maximum is observed for all the other samples, as seen for $x = 2$. The fact that these curves depart so much from each other at intermediate to high temperature makes it difficult to separate the magnetic contribution by subtracting the data for a nonmagnetic compound of the AB_2O_6 family. Additionally, due to the structure's complexity (nine atoms per unit cell), the high-temperature specific heat is dominated by a large number of optical modes, which are expected to be frozen at low temperatures, so that the acoustic modes are the ones that need to be subtracted to extract the magnetic contribution, and these are better described by the Debye model. We then resorted to a procedure that consists in subtracting from the total specific heat curve a Debye-model contribution, which is given by

$$C_D(T) = 9R\left(\frac{T}{\Theta_D}\right)^3 \int_0^{\Theta_D/T} \frac{x^4\, e^x}{(e^x - 1)^2}\, dx, \qquad (3)$$

where R is the gas constant, and Θ_D is the Debye temperature. This is the only adjustable parameter, which we choose so as to have a touching point between the data and this curve. The touching point of the curves, exemplified in the bottom panel of Fig. 7, coincides with the inflection of the Debye curve, where it starts to stabilize toward its high-temperature limit of $3R$, while the full specific heat continues to grow up to its high-temperature limit of $27R$. The values of Θ_D were found to vary from slightly below 190 K to slightly above 220 K throughout the series of compounds. One should be

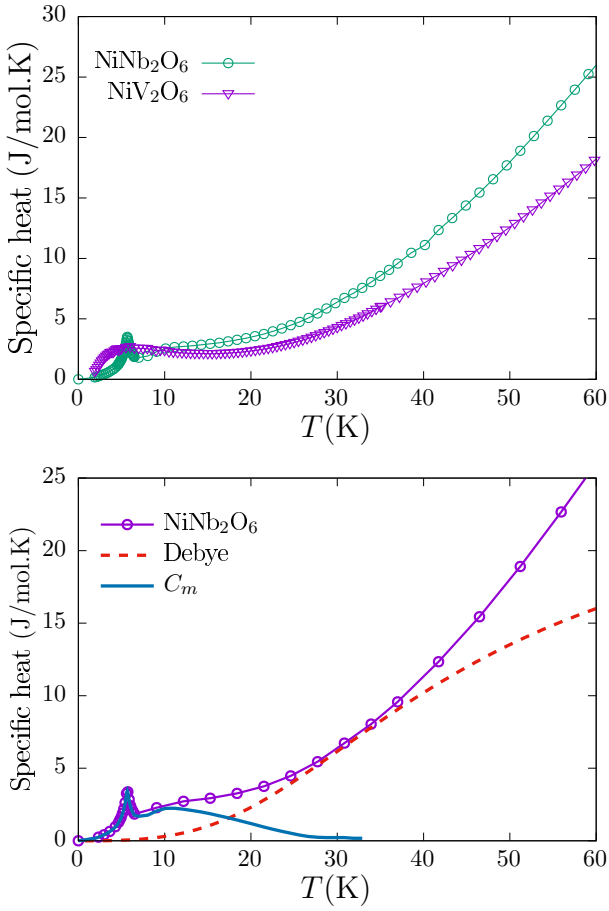

FIG. 7. (a) Specific heat as a function of the temperature for samples $x = 0$ and 2. (b) Example of extraction of the magnetic specific heat by subtracting a Debye-model contribution, as explained in the text.

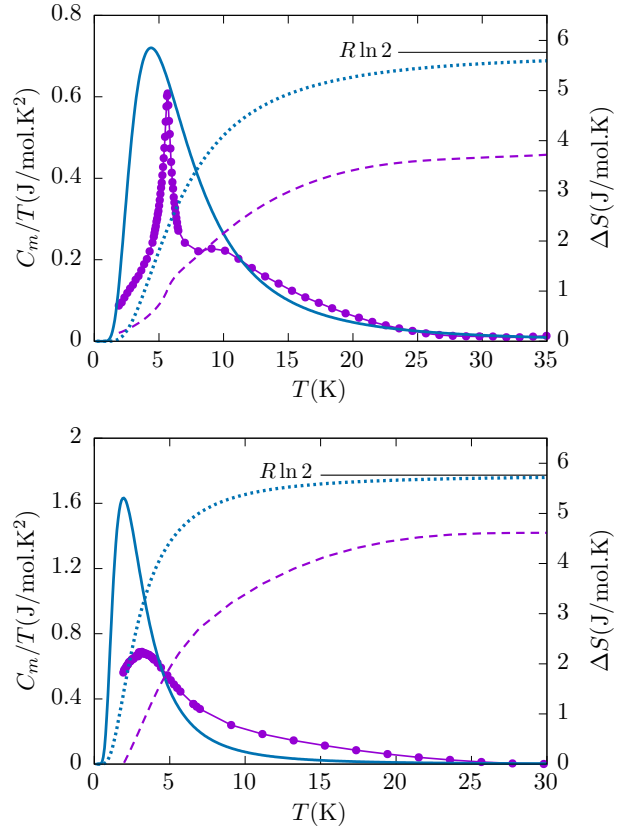

FIG. 8. Magnetic specific heat of the samples $NiNb_2O_6$ (top) and $NiNbVO_6$ (bottom), plotted as C_m/T vs T (crossed lines), and the corresponding amount of entropy ΔS obtained from its numerical integration (dashed lines). The theoretical specific heat (continuous line) and entropy (dotted line) for isolated Ising chains are included for comparison.

aware that this procedure is not rigorous, since we can see in Fig. 7 that the magnetic contribution is being reduced, but still present, when the lattice contribution already begins to depart from a simple Debye model due to the large number of optical-phonon branches.

With the magnetic specific heat (C_m) determined as described above, Fig. 8 shows two representative plots of C_m/T as a function of the temperature T, together with the temperature integral of this ratio, which gives the change of magnetic entropy ΔS across the integration interval. We also include the theoretical specific heat of isolated Ising chains [31],

$$C_m^{\mathrm{ch}}(T) = R\left(\frac{J_0}{T}\right)^2 \mathrm{sech}^2\left(\frac{J_0}{T}\right), \tag{4}$$

as well as the corresponding ΔS. We used the intrachain exchange constant J_0 obtained from the susceptibility analysis (Table II). Clear indications of the presence of Ising chains can be seen in the plots of Fig. 8, although it is also clear that interchain interactions induce a longer tail of $C_m(T)$ at higher temperatures, with the corresponding reduction of height of the peak that denotes the one-dimensional character of the Ni-chains. We also see that the entropy, although reasonably preserved for $x = 1$, is quite deficient for $x = 0$. In contrast, the latter clearly shows a magnetic-transition peak, which is absent in the former, even though a magnetic transition was clearly indicated by the susceptibility analysis. This is not an unusual observation in specific-heat measurements. It is possible that the full weight of the peak is missed due to incomplete relaxation in the vicinity of the transition.

We wish to point out that the entropy limits shown in Fig. 8 are consistent with the expected value $R\ln 2$ for a two-state Ising-like spin. We found this to hold for $NiNb_2O_6$, NiV_2O_6, and $NiNbVO_6$. In contrast, for $x = 0.66$ and 1.5 the entropy limit falls between $R\ln 2$ and $R\ln 3$. For these two samples, Nb and V ions cannot alternate regularly along a chain, so that a certain amount of disorder in the occupation of the B cation is expected. This affects the distortions of the oxygen octahedra surrounding the magnetic ion in a way that reduces the uniaxial spin anisotropy. Then, even if a full rotationally invariant Heisenberg system were not recovered, the frozen $S_z = 0$ state could be thermally activated. This is an interesting perspective because it would not invalidate our evaluation of the exchange parameters using Eqs. (1) and (2), as J_0 is essentially determined by the low-temperature rise of $\chi(T)$.

IV. CONCLUSIONS

We analyzed changes in the low-dimensional magnetism of a family of compounds NiB_2O_6 that are due to structural

modifications promoted by chemical substitution on the *B* site. The starting point was the successful synthesis of a series of samples of $NiNb_{2-x}V_xO_6$, varying the vanadium concentration while maintaining the *Pbcn* crystal structure of the niobate. For samples with $x > 0$, this structure was stabilized under extreme HPHT conditions. We found that the unit-cell volume is reduced by 11% when the vanadium content goes from $x = 0$ to 2. However, this change is not isotropic, as lattice parameters shrink sensibly less along the *b* axis than along the *a* or *c* axes.

With regard to intrinsic magnetic properties of these compounds, our analysis reveals that FM intrachain superexchange interactions are dominant, remaining one order of magnitude larger than AF interchain couplings along the whole series of $NiNb_{2-x}V_xO_6$ samples. Although the smaller size and effective charge of vanadium with respect to niobium induce structural changes in the local environment of Ni^{2+} ions, this does not alter their magnetic moment along the series. However, the increase of the Ni-O distance strongly reduces FM interactions along the 1D chains, as deduced from the drastic reduction of the intrachain exchange constant J_0. In contrast, AF interchain interactions vary within a much narrower range. Overall, this tends to lower the transition temperature to long-range magnetic ordering as the vanadium content increases.

Within the ordered phase, we observe a metamagnetic transition at critical fields $\mu_0 H \gtrsim 1$ T, which we interpret as a spin-flip transition between antiferromagnetically oriented FM chains to overall FM order. This transition is smoothed out due to the polycrystalline nature of the samples, and it becomes barely visible for intermediate composition due to disorder in the occupation of the *B* site.

Finally, our specific-heat measurements, despite the difficulties in separating the magnetic contribution, have lent support to the picture of weakly interacting Ising-like chains that emerged from our analysis of susceptibility and magnetization data. In particular, the most clearly defined peak in the specific heat, occurring for $NiNb_2O_6$, coincides with the Néel temperature previously determined from the magnetic susceptibility. The estimated magnetic entropy is consistent with our description of the Ni^{2+} magnetic moments as Ising spins. Furthermore, the consistency of our interpretation is confirmed by a comparison of the magnetic specific heat with theoretical predictions for independent Ising chains with the same intrachain exchange values determined from the susceptibility.

Further measurements, with other techniques like neutron diffraction, as well as synthesis of single crystals of the HPHT-stabilized structure, are needed in order to control anisotropy properties and further elucidate the nature of magnetic phases along the series of $NiNb_{2-x}V_xO_6$ compounds.

ACKNOWLEDGMENTS

This work was financed by the French-Brazilian cooperation program CAPES-COFECUB, process 88887.321681/2019-00, and the French institution Centre National de la Recherche Scientifique, CNRS. We thank the professional team of the X-Press pole of Institut Néel, especially Murielle Legendre and Céline Goujon, for technical support with the preparation of the samples.

[1] E. G. Santos, S. R. de Oliveira-Neto, E. J. Kinast, J. B. M. da Cunha, O. Isnard, and M. A. Gusmão, Magnetic phases of the quasi-two-dimensional compounds $Fe_xCo_{1-x}Ta_2O_6$, J. Phys.: Condens. Matter **22**, 496004 (2010).

[2] S. R. de Oliveira Neto, E. J. Kinast, M. A. Gusmão, C. A. dos Santos, O. Isnard, and J. B. M. da Cunha, X-ray diffraction and magnetic susceptibility measurements for $Fe_xNi_{1-x}Ta_2O_6$, J. Phys.: Condens. Matter **19**, 356210 (2007).

[3] Y. Muraoka, T. Idogaki, and N. Uryu, Susceptibility analysis of two-dimensional antiferromagnet $FeTa_2O_6$, J. Phys. Soc. Jpn. **57**, 1758 (1988).

[4] R. Coldea, D. A. Tennant, E. M. Wheeler, E. Wawrzynska, D. Prabhakaran, M. Telling, K. Habicht, P. Smeibidl, and K. Kiefer, Quantum criticality in an ising chain: Experimental evidence for emergent e8 symmetry, Science **327**, 177 (2010).

[5] T. Liang, S. M. Koohpayeh, J. W. Krizan, T. M. McQueen, R. J. Cava, and N. P. Ong, Heat capacity peak at the quantum critical point of the transverse Ising magnet $CoNb_2O_6$, Nat. Commun. **6**, 7611 (2015).

[6] S. Lee, R. K. Kaul, and L. Balents, Interplay of quantum criticality and geometric frustration in columbite, Nat. Phys. **6**, 702 (2010).

[7] P. W. C. Sarvezuk, E. J. Kinast, C. V. Colin, M. A. Gusmão, J. B. M. da Cunha, and O. Isnard, New investigation of the magnetic structure of $CoNb_2O_6$ columbite, J. Appl. Phys. **109**, 07E160 (2011).

[8] P. W. C. Sarvezuk, M. A. Gusmão, J. B. M. da Cunha, and O. Isnard, Magnetic behavior of the $Ni_xFe_{1-x}Nb_2O_6$ quasi-one-dimensional system: Isolation of Ising chains by frustration, Phys. Rev. B **86**, 054435 (2012).

[9] M. L. Hneda, J. B. M. da Cunha, M. A. Gusmão, S. R. Oliveira Neto, J. Rodríguez-Carvajal, and O. Isnard, Low-dimensional magnetic properties of orthorhombic MnV_2O_6: A nonstandard structure stabilized at high pressure, Phys. Rev. B **95**, 024419 (2017).

[10] M. Lenertz, J. Alaria, D. Stoeffler, S. Colis, and A. Dinia, Magnetic properties of low-dimensional α and γcov_2o_6, J. Phys. Chem. C **115**, 17190 (2011).

[11] M. Markkula, A. M. Arevalo-Lopez, and J. Paul Attfield, Neutron diffraction study of monoclinic brannerite-type CoV_2O_6, J. Solid State Chem. France **192**, 390 (2012).

[12] M. Lenertz, J. Alaria, D. Stoeffler, S. Colis, A. Dinia, O. Mentré, G. André, F. Porcher, and E. Suard, Magnetic structure of ground and field-induced ordered states of low-dimensional α-CoV_2O_6: Experiment and theory, Phys. Rev. B **86**, 214428 (2012).

[13] T. Hanawa, K. Shinkawa, M. Ishikawa, K. Miyatani, K. Saito, and K. Kohn, Anisotropic specific heat of $CoNb_2O_6$ in magnetic fields, J. Phys. Soc. Jpn. **63**, 2706 (1994).

[14] C. Heid, H. Weitzel, F. Bourdarot, R. Calemczuk, T. Vogt, and H. Fuess, Magnetism in $FeNb_2O_6$ and $NiNb_2O_6$, J. Phys.: Condens. Matter **8**, 10609 (1996).

[15] S. Kobayashi, S. Mitsuda, M. Ishikawa, K. Miyatani, and K. Kohn, Three-dimensional magnetic ordering in the quasi-one-dimensional Ising magnet $CoNb_2O_6$ with partially released geometrical frustration, Phys. Rev. B **60**, 3331 (1999).

[16] M. Belaıhe, M. Bakhache, M. Drillon, A. Derrory, and S. Vilminot, Magnetic properties of MV_2O_6 compounds (M=Cu, Co, Ni), Physica B **305**, 270 (2001).

[17] M. L. Hneda, J. B. M. da Cunha, A. Popa, and O. Isnard, Magnetic order suppression and structural characterization of $MnNb_{2-x}V_xO_6$ columbites crystallized under extreme pressure conditions, J. Magn. Magn. Mater. **496**, 165907 (2020).

[18] Z. Chuan-Cang, L. Fa-Min, D. Peng, C. Lu-Gang, Z. Wen-Wu, and Z. Huan, Synthesis, structure and antiferromagnetic behavior of brannerite MnV_2O_6, Chin. Phys. B **19**, 67503 (2010).

[19] S. A. J. Kimber and J. P. Attfield, Disrupted antiferromagnetism in the brannerite MnV_2O_6, Phys. Rev. B **75**, 064406 (2007).

[20] H. X. Dang, A. J. E. Rettie, and C. B. Mullins, Visible-light-active niv_2o_6 films for photoelectrochemical water oxidation, J. Phys. Chem. C **119**, 14524 (2015).

[21] J. Ye, Z. Zou, and A. Matsushita, A novel series of water splitting photocatalysts NiM_2O_6(M = Nb, Ta) active under visible light, Int. J. Hydrogen Energy **28**, 651 (2003).

[22] M. E. Arroyo y de Dompablo, Y.-L. Lee, and D. Morgan, First principles investigation of oxygen vacancies in columbite MNb_2O_6 (M = Mn, Fe, Co, Ni, Cu), Chem. Mater. **22**, 906 (2010).

[23] A. Orera, F. Garcia-Alvarado, and J. T. S. Irvine, Effect of Ti-substitution on the electrical properties of $MnNb_2O_{6-\delta}$, Chem. Mater. **19**, 2310 (2007).

[24] R. Tang, Y. Li, S. Xie, N. Li, J. Chen, C. Gao, P. Zhu, and X. Wang, Exploring the coordination change of vanadium and structure transformation of metavanadate MgV_2O_6 under high pressure, Sci. Rep. **6**, 38566 (2016).

[25] J. Peña, P. Bouvier, and O. Isnard, Structural properties and Raman spectra of columbite-type $NiNb_{2-x}V_xO_6$ synthesized under high pressure, J. Solid State Chem. **291**, 121607 (2020).

[26] J. Rodríguez-Carvajal, Recent advances in magnetic structure determination by neutron powder diffraction, Physica B **192**, 55 (1993).

[27] A. Barlet, J. Genna, and P. Lethuillier, Insert for regulating temperatures between 2 and 1000 K in a liquid helium dewar: Description and cryogenic analysis, Cryogenics **31**, 801 (1991).

[28] P. W. C. Sarvezuk, E. J. Kinast, C. V. Colin, M. A. Gusmão, J. B. M. da Cunha, and O. Isnard, Suppression of magnetic ordering in quasi-one-dimensional $Fe_xCo_{1-x}Nb_2O_6$ compounds, Phys. Rev. B **83**, 174412 (2011).

[29] J. B. Goodenough, Book review: Magnetism and the chemical bond: J. B. Goodenough, (Wiley, London, 1963, xv-393 p. 95 s), Nucl. Phys. **50**, 693 (1964).

[30] H. Zhang, D. Zeng, and Z. Liu, The law of approach to saturation in ferromagnets originating from the magnetocrystalline anisotropy, J. Magn. Magn. Mater. **322**, 2375 (2010).

[31] D. C. Mattis, *The Theory of Magnetism*, international edition (Harper & Row, New York, 1965).